Journal of Materials Chemistry A, Volume 7, Issue 15, April 2019, pp. 9173-9182
DOI: 10.1039/C9TA01237K

Synthesis of highly effective stabilized-CaO sorbents via a sacrificial N-doped carbon nanosheet template

Ke Wang[1,2], Peter T. Clough[2], Pengfei Zhao[1], Edward J. Anthony[2*]

[1] School of Electrical and Power Engineering, China University of Mining and Technology, Xuzhou 221116, China.

[2] Energy and Power Theme, Cranfield University, Cranfield, Bedfordshire, MK43 0AL, UK.

Ke Wang is currently visiting Cranfield University.

* Corresponding author: Edward J. Anthony, E: b.j.anthony@cranfield.ac.uk, T: +44 (0) 1234 752 823

Abstract: Calcium looping, a promising high-temperature CO_2 capture technique, offers a midterm economic solution to mitigate anthropogenic CO_2 emissions. The main challenge for calcium looping is the synthesis of highly efficient CaO-based sorbents that can be used over many reaction cycles. Here, a sacrificial N-doped carbon nanosheet template was developed which produces MgO-stabilized, CaO sorbents with fast adsorption rates, high capacities and remarkable long term performance over many cycles. The characterization results show that such a template was formed through *in situ* pyrolysis of an organic acid and nitrates in a simple heating process under nitrogen. The presence of a carbonaceous template prevented crystallite growth, featured a highly macroporous nanosheet (~60 nm thick) morphologies, and ensured homogeneously mixing of Ca and Mg, which is essential to minimize diffusion limitations, mitigate sintering, and produce structural stabilization. Thus, 10 mol% MgO acting as an inert stabilizer was sufficient to achieve a CO_2 uptake of 0.65 g/g (corresponding to a capacity retention of 89.9%) after 10 cycles in realistic conditions, as confirmed by TGA analyses. This N-doped carbon template can be applied generally to form a wide range of porous and nanostructured stabilized-CaO sorbents with stable CO_2 uptakes.

Keywords: CO_2 capture, CaO sorbent, N-doped carbon, Sacrificial template.

Introduction

Global warming is receiving increasing attention, as anthropogenic CO_2 emissions, mainly produced by the combustion of fossil fuels, continue to rise.[1] Carbon capture and sequestration (CCS) is one of the most cost-effective approaches to reduce CO_2 emissions in the short to midterm.[2] The key step for CCS lies in the capture process, which accounts for 60−70% of the total cost.[3] The capture process for classical amine scrubbing technique are relatively expensive due to the cooling requirement for the hot flue gases, which is accompanied by large energy losses.[4] Alternative approaches involve developing intermediate-temperature and high-temperature sorbents, which can directly trap CO_2 from hot flue gases, and thus reduce the cost of CO_2 capture to more commercially acceptable levels.[5] Numerous types of sorbents including hydrotalcites[6, 7], calcium oxides[8-11], and ceramic materials[12-15] have been studied. Calcium oxides in the form of calcium looping (CL) technology are considered to be one of the most promising candidates among these materials owing to (i) abundant naturally occurring CaO precursors (e.g. limestone or dolomite), (ii) high theoretical CO_2 uptake capacity (approximately 0.78 g CO_2/g CaO), and (iii) the environmentally friendly characteristics of lime based sorbents[16-19].

However, the main drawback of limestone-derived CaO sorbents is the rapid decay in CO_2 uptake capacity with repeated carbonation/calcination cycles. This poor cyclic stability is typically explained by sintering-induced significant loss of meso-porosity and surface area since the low Tammann temperature (T_T) of $CaCO_3$ (~529 °C) is below typical operating temperatures for such a cycle (600-700 °C for carbonation and 900-950 °C for calcination).[20, 21] To mitigate severe sintering, a number of thermal/chemical treatments, including hydration[22, 23], self-reactivation[24, 25], re-carbonation[26, 27], doping[28], acidification[29, 30], and biomass templating[31-34] have been investigated to increase the porosity of raw CaO. Another approach is to stabilize the CaO structure by using high-T_T stabilizers (i.e. MgO[25, 35-37],

Al_2O_3[38-42], ZrO_2[43-45], and CeO_2[46]).

The size of the CaO grains/particles also play an equally crucial role in the CO_2 uptake of CaO sorbents. It is accepted that the carbonation reaction proceeds through an initial rapid chemically reaction stage followed by the slow diffusion-controlled reaction stage.[47] The transition between the two stages occurs once the $CaCO_3$ layer reaches a critical thickness (~50 nm).[48] Due to the short gas–solid residence times in practice, the slow diffusion reaction stage has to be avoided, and the ideal CaO grain size should be < 100 nm.[49]

Based upon these criteria outlined above, porous nanostructured stabilized-CaO offer a favorable morphology for high-performance CaO sorbents. To obtain this favorable morphology, one simple strategy is to coat the surfaces of nanosized $CaCO_3$ particles with stabilizers.[50, 51] As an alternatively, nanostructured CaO can be inversely grafted onto refractory macro/mesoporous supports.[52-54] However, these procedures lack the ability to tailor the textural properties or requires a relatively large account of inert stabilizer. Recently, template-assisted synthesis has emerged as a method to design porous core–shell nanostructured CaO-based sorbents, composed of a refractory thin shell and active nanosized CaO-riched core. Liu et al.[55] synthesized mesoscopic hollow CaO@$Ca_{12}Al_{14}O_{33}$ spheres using sulfonated polystyrene as hard templates. Here the "@" symbol represents a core-shell structure. Broda et al.[56] prepared a hollow Al_2O_3-stabilized micro-spheres via a sacrificial carbon gel templating technique. Ping et al.[57] facilitated ZrO_2-stabilized CaO hollow spheres employing colloidal carbon as a template. Armutlulu et al.[58] produced multishelled CaO@MgO microspheres through a template-assisted hydrothermal route. Despite those impressive results, previous studies using template-assisted synthesis still suffer from complex synthetic procedures or the use of expensive instrumentation, which cannot be easily scaled up.

Here, we have developed highly macroporous MgO-stabilized CaO nanosheets via a

novel N-doped carbon sheets template route. The sacrificial template was formed through *in situ* pyrolysis of commercially available D-Glucose acid and nitrates in a simple heating process under nitrogen (N_2), further acting as a CaO dispersant during burn-off in the secondary calcination step under air. The whole procedure is rather simple, cost-effective and scalable. This N-doped carbon template can also be applied generally to produce a wide range of porous and nanostructured stabilized-CaO sorbents. More importantly, the structural and morphology characteristics of synthesized sorbents were evaluated to elucidate the formation mechanism of N-doped carbon sheets template. To simulate the practically relevant operating conditions,[59] the cyclic CO_2 capture performance was tested under a realistic calcination conditions (at 950 °C in 100% CO_2).

Experimental

Reagents and Materials

All of the reagents used in this paper were obtained from Shanghai Aladdin Reagent Co., China. Analytical grade calcium nitrate tetrahydrate ($Ca(NO_3)_2 \cdot 4H_2O$) was used as the calcium based precursor. D-Glucose acid solution (49~53 wt% in water) was used for template carbon source. Analytical grade magnesium nitrate hexahydrate ($Mg(NO_3)_2 \cdot 6H_2O$), aluminum nitrate nonahydrate ($Al(NO_3)_3 \cdot 9H_2O$), cerium nitrate hexahydrate ($Ce(NO_3)_3 \cdot 6H_2O$), and zirconium oxynitrate hydrate ($ZrO(NO_3)_2 \cdot xH_2O$) were used as metal oxide precursor.

Preparation of Sorbents

Sorbents were synthesized via a cost-effective carbon sacrificial templating technique. Firstly, an appropriate amount of calcium nitrate tetrahydrate (12.7 mmol) as calcium precursor was dissolved in deionized water (150 ml). Subsequently, D-Glucose acid solution was added to the mixture (the molar ratio of calcium to acid was 2/1). Then the metal oxide precursor (1.4 mmol; $Mg(NO_3)_2 \cdot 6H_2O$, $Al(NO_3)_3 \cdot 9H_2O$, $Ce(NO_3)_3 \cdot 6H_2O$ or

$ZrO(NO_3)_2 \cdot xH_2O$) was added and the molar ratio of calcium to metal ion was set at 9/1. The solution was stirred by a magnetic stirrer at 80 °C for 6 h, and then dried in an oven at 70 °C overnight. After drying, the material was pyrolyzed in a horizontal tubular furnace under N_2 flow (200 mL/min) at 600 °C (ramp 5 °C/min) for 2 h. Then the atmosphere was switched to air, and the tubular furnace was heated to 800 °C (ramping rate of 5 °C/min), the temperature was maintained for 2 h to produce fresh sorbents. For comparison, the direct calcination method was used as following: the material obtained after drying was calcined directly in an air atmosphere at 800 °C (ramp 5 °C/min) for 2 h. To compare with using calcium nitrate, calcium carbonate was also used in both methods as precursor.

To describe the composition, the following nomenclature is used: In the first part, "CaN" or "CaC" represents calcium nitrate or calcium carbonate as precursors, respectively. While, "Mg", "Al" "Ce" or "Zr" represent the MgO, Al_2O_3, Ce_2O_3 or ZrO_2 inert used as stabilizers. These were added in the form of metal nitrate with a molar ratio of calcium to metal stabilizer of 9/1. Here, A represents a direct calcination method, the blank indicates a carbon template method, and U means a carbon template method without sorbents being calcined in air at 800 °C for 2 h. For example, the CaN-Mg refers to a sorbent which was obtained by a carbon template method using calcium nitrate as the precursor with the MgO stabilizer addition.

Characterization

X-ray diffraction (XRD) on the sorbents was performed using a Rigaku D/max2550 X-ray diffractometer to determine the phase composition. The operating parameters were Cu Kα target (λ = 0.154056 nm) and 40 kV/100 mA power generator. A scan range of 10-80° (2θ) was measured with a step size of 0.02° and speed 0.1 sec/step. The size and morphology of the sorbents were characterized via scanning electron microscope (SEM: JSM-6360LV), transmission electron microscopy (TEM: JEM-2010) and energy dispersive spectrometer (SEM-mapping: EDAX Genesis Apex 2 system). The chemical valence states on the surface

was analyzed using X-ray photoelectron spectroscopy (XPS: Perkin-Elmer, PHI 5600). Specific surface area (BET) and desorption average pore diameter (BJH) analyses were conducted by means of a NOVA 2000 Quantachrome instrument.

Performance Tests of Sorbents

The carbonation/calcination looping reactions were tested using a thermogravimetric analyzer (ZRY-1P, Techcomp Jingke Scientific Instrument Co., Ltd., Shanghai, China). During each run, sorbents (approximately 5 mg) was placed in an alumina crucible. Prior to each cycling test, sorbents were calcined at 850 °C (ramp up 15 °C/min) in N_2 flow (50 mL/min) for 5 min. Then the temperature was decreased to 700 °C (ramp down 15 °C/min), and the looping test started with carbonation process (15% CO_2 in N_2 at 700 °C for 20 min). After carbonation, the gas was switched to 100% CO_2, and the sorbent was heated to 950 °C at a rate of 10 °C/min for a 5 min calcination. This cycling process was repeated 10 times.

Results and Discussion

3.1 Unsupported CaO sorbents

Fig. 1 shows the XRD patterns of two pure CaO sorbents prepared by a carbon template (CaN) and a direct calcination (CaN-A) method. As expected, the highly crystalline CaO was identified in both samples, indicating that the sorbents derived from two different calcination conditions have identical crystalline phases. However, the intensities of CaO peaks were significantly different. The average crystallite size of CaO was further estimated using the Scherrer's equation: $D\ (nm) = k\lambda/\beta \cos\theta$, where k is the Scherrer constant (k=0.89), λ is the wavelength of X-rays (λ=0.015 nm), β is the full width at half maximum, and θ is the diffraction angle. The calculated crystal size of CaO is shown in Table 1. The crystal size of CaN is 31.6 nm, which is smaller than CaN-A (34.3 nm). Similar to CaO sorbents derived from organometallic calcium-based carbon template route,[60] the carbon formed during carbonization process under N_2 atmosphere serves as a physical dispersant to effectively

prevent crystal growth of CaO as compared with the case of sorbents produced under an air atmosphere. The SEM images of these two CaO sorbents are further shown in Fig. 2. The CaN-A (Fig. 2a) appeared as a thick "flaky-like" structure with a relatively porous surface as well as large and compact aggregates (inset picture). While CaN (Fig. 2b) presented a well-developed porous nanosheet-like morphology containing twisted and separated filaments of peanut-shaped particles. This architecture is remarkably similar to the structure of the templated carbonized sample (Fig. 2c), which possessed a nanosheet-like structure with nonporous surface. Intriguingly, the presence of nanosheeted carbon template effectively impeded the agglomeration of CaO. Moreover, burning the carbon template further contributed to induce improved porous morphology as supported by N_2 adsorption results. Table 2 revealed that the specific surface area, pore volume, and average pore size of CaN were relatively larger than those of CaN-A. The above analyses clearly demonstrate that the physical-chemical properties of CaO depend strongly on the presence of nanosheeted carbon template under a N_2 atmosphere.

Table 1 The crystal sizes of CaO calculated by Scherrer Equation

Sorbents	CaN-A	CaN	Ca-Mg-A	Ca-Mg	Ca-Al	Ca-Ce	Ca-Zr
Size (nm)	34.3	31.6	29.4	26.9	31.4	29.7	45.9

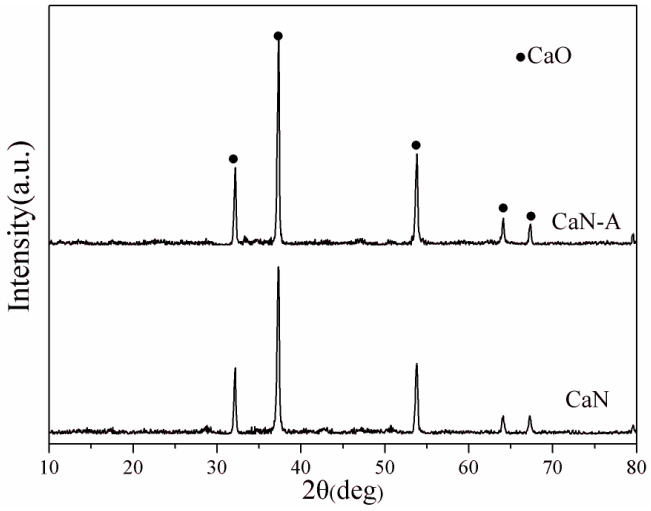

Fig. 1 XRD patterns of prepared samples.

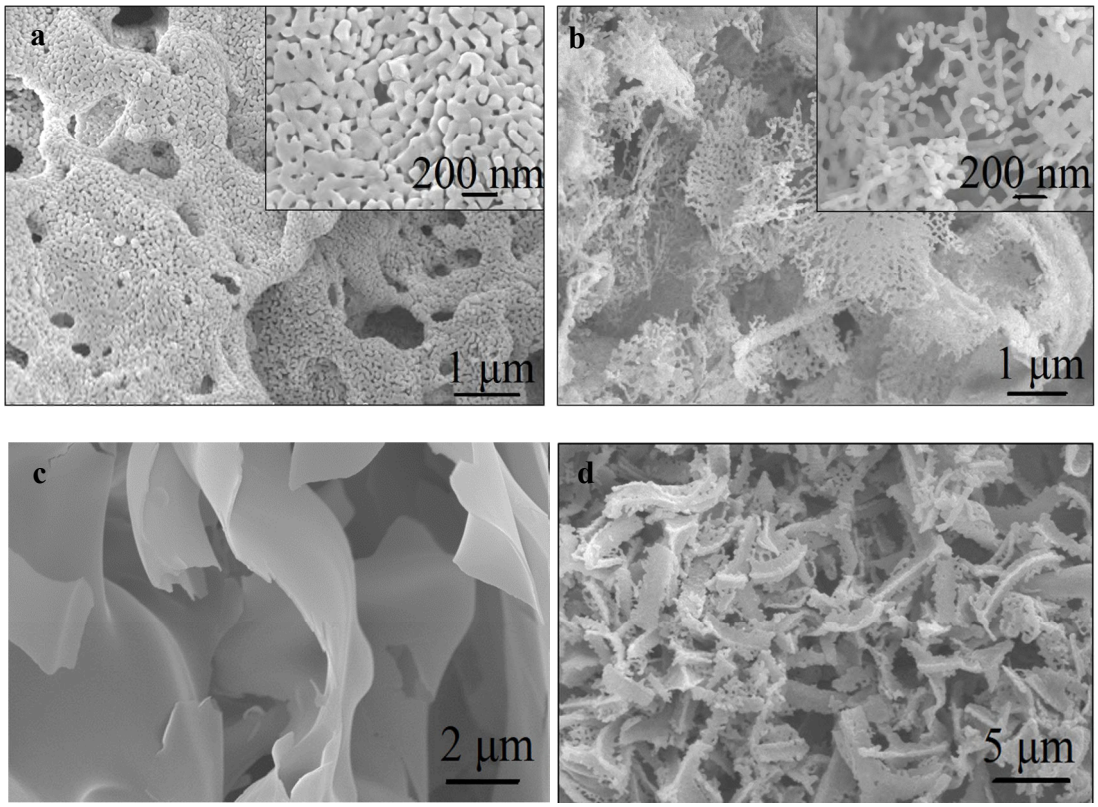

Fig. 2 SEM images of sorbents: (a) CaN-A, (b) CaN, (c) CaN-U, (d) CaC.

Table 2 Properties of different prepared sorbents

Sample	surface area (m^2/g)	pore volume (cm^2/g)	average pore size (nm)
CaN	11.40	0.110	23.6
CaN-A	9.52.	0.0906	21.7
Ca-Mg	12.95	0.186	29.5

To elucidate the underlying mechanism for the formation of nanosheeted carbon template, its composition was determined using XRD, elemental analysis and XPS. XRD patterns (Fig. 3a) showed that the main crystalline phase was $CaCO_3$. It seems that calcium nitrate reacted with gluconic acid to form $CaCO_3$ during the carbonization process. There was also an amorphous characteristic C (002) peaks at around 15 degrees, suggesting char carbon was being produced. Such $CaCO_3$/C composite product contains C, O, H, and N (Fig. 3b), and suggests that N is being introduced into the resulting carbon product during pyrolysis of the mixture (gluconic acid and calcium nitrate). XPS analysis was further performed to determine the chemical composition. The survey spectra were scanned in the range 0-1350

eV (Fig. 3c). The presence of C 1s (285.1 eV), O 1s (531.2 eV), Ca 1s (358.5 eV) and N 1s (409.8 eV) was detected, which is in agreement with XRD and the elemental analysis. In particular, the high-resolution N 1s spectrum (Fig. 3d) confirms the structural N atoms in the form of pyridinic, pyrrolic, and graphitic C–N bonds, which are very similar to that of typical N-doped graphene.[61] However, this sample appears to have no NO_x species (~406 ev), indicating that the strong oxidizing NO_x species does not survive during carbonization process (reducing environment). This suggests that the nitrogen in the solid matrix stays bound into the carbon framework.

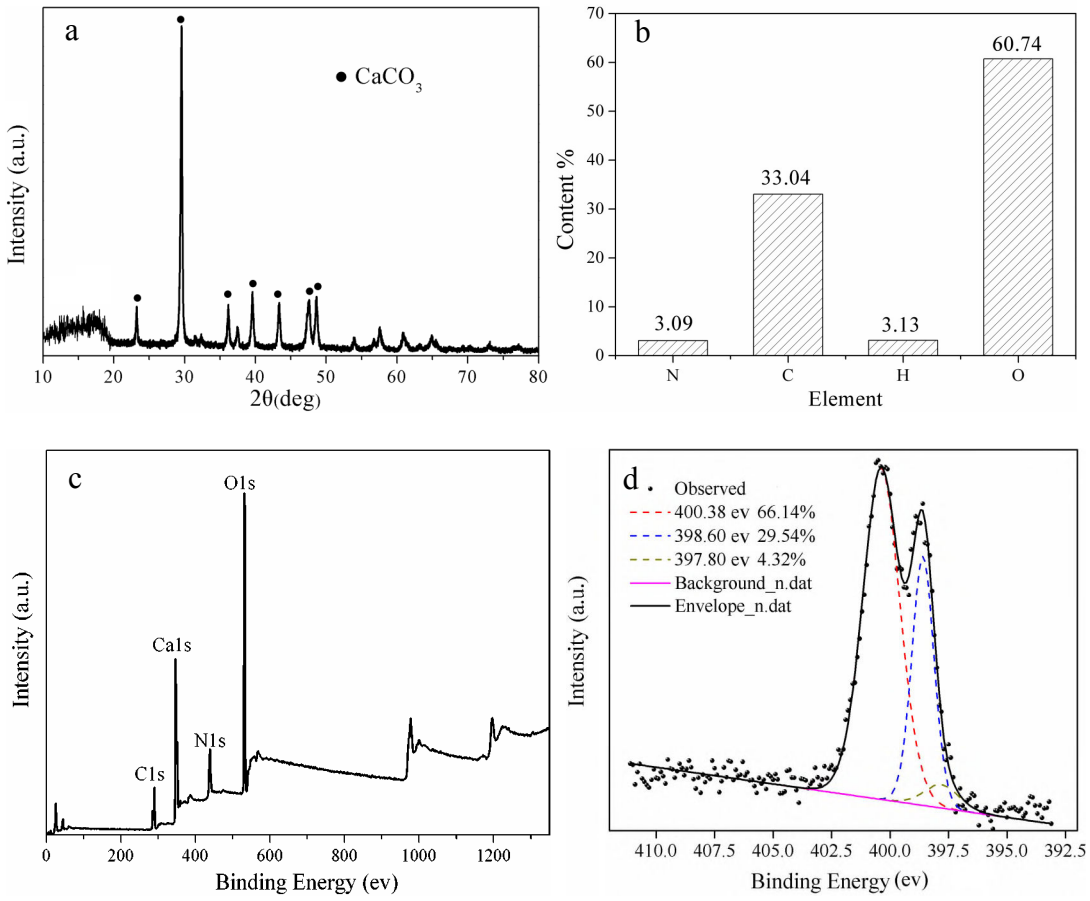

Fig. 3 (a) XRD pattern, (b) Element content distribution, (c) XPS spectrum, (d) The high-resolution N 1s spectrum.

The microstructures of the N-doped carbon template were further observed by SEM images. The reference material, with an undoped carbon template is produced by simply

replacing $Ca(NO_3)_2$ with $CaCO_3$ (in the same molar ratio) and is used to provide a comparison. Both carbonaceous template (after pyrolysis at 600 °C in N_2) are predominantly in the form of a thin lamellar architectures as shown in Fig. 4a-b. These carbon sheets have a clearly two-dimensional (2D) structure with typical thicknesses of 20–50 nm. In particular, N-doped carbon template was thinner than the undoped carbon template. Fig. 4b further reveals that $CaCO_3$ nanoparticles (as supported by XRD results) are primarily formed at the junction points of neighboring carbon material. Surprisingly, the average size of $CaCO_3$ nanoparticles (~5 nm) in N-doped carbon template is only quarter that of the undoped carbon template (~20 nm), indicating that N-doped carbon acted as a more effective barrier to separate the $CaCO_3$ nanoparticles than undoped carbon. When calcination of these templates in air, the SEM imagines of their CaO products are shown in Fig. 2b and Fig. 2d. The sheet-like architecture is maintained in the two sorbents. However, compared with the case of CaC (Fig. 2d), a more macroporous morphology containing smaller nano-sized particles was obtained in CaN (Fig. 2b). These findings suggest that the morphology of the final product is also significantly affected by its nanosheeted carbon template's morphology. It is the thinner N-doped carbon nanosheet template with smaller $CaCO_3$ nanoparticles, which produced a more favorable morphology for a CaO sorbent.

Fig. 5 gives the cyclic CO_2 capture performance of three CaO sorbents in a TGA for 10 carbonation/decarbonation cycles under severe calcination conditions. Here, the initial CO_2 uptake capacity of CaN-A is only 0.573 g CO_2/g sorbent, which appears to be due to the relatively compact and large CaO aggregates (Fig. 2a). In comparison, the first CO_2 uptake capacity of CaC increases to 0.640 g/g, indicating that the presence of nanosheeted carbon template led to a porous sheet-like structure (Fig. 2d), leading in turn to improve CO_2 uptake capacity. When further using the N-doped carbon nanosheet template, the CO_2 uptake capacity of CaN becomes as high as 0.705 g/g during the first cycle due to its more

macroporous nanosheet morphology with smaller nano-sized CaO particles (Fig. 2b), and remains higher over the entire 10 cycles.

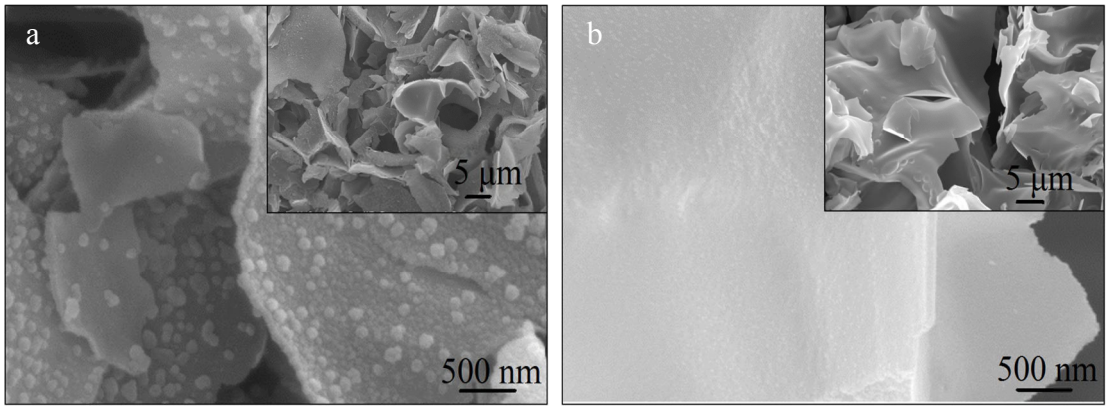

Fig. 4 SEM images of sorbents: (a)CaC-U, (b)CaN-U.

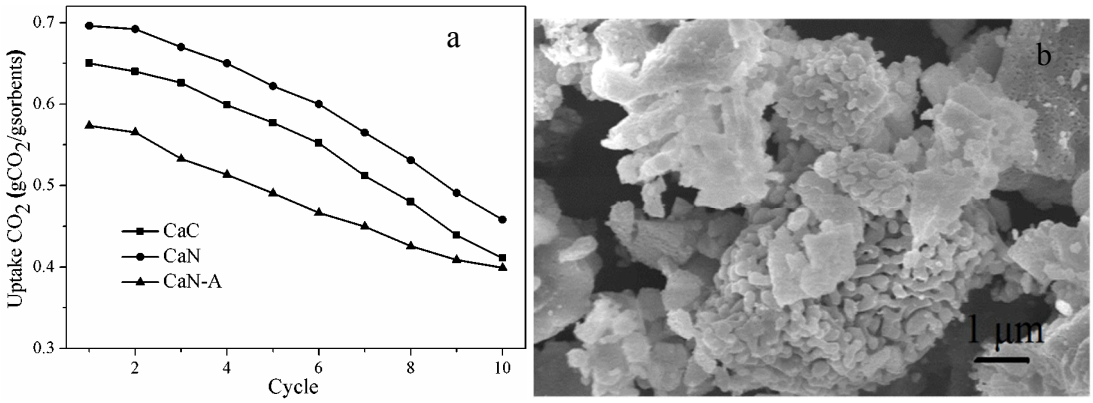

Fig. 5 (a) Cyclic CO_2 capture results of sorbents over 10 cycles and (b) the SEM imagine of cycled CaN after 10 cycles.

Although all CaO sorbents demonstrate a decay in sorption capacity, CaN was the best among the three CaO sorbents. This decay was due to particles agglomeration and sintering as confirmed by the morphology of cycled CaN (Fig. 5b). This result highlights the fact that the unique macroporous nanosheet morphology breaks down during the 10 cycles and must eventually cease to serve as a structural stabilizer.

3.2 MgO-stabilized CaO sorbents

To improve the cyclic stability of CaN, MgO as an inert stabilize in the form of metal nitrate was added via the N-doped carbon nanosheet template method. The molar ratios of Ca to inserted metal ion are fixed at 9/1. Fig. 6 compares the XRD patterns of the three samples.

The main crystalline of Ca-Mg-U is $CaCO_3$. Here, there are also amorphous characteristic C (002) peaks at around 15 degrees, demonstrating the formation of carbon template in carbonization process. Furthermore, as shown in Table 1, the CaO crystal sizes of Ca-Mg (26.9 nm) was slightly smaller than Ca-Mg-A (29.4 nm), proving that the carbonization process inhibited the growth of CaO crystal sizes. Interestingly, the phase of MgO could not be detected by XRD but its presence was shown by XPS results (Fig. 9b). It is therefore reasonable to speculate that MgO is present as an amorphous phase, which is in agreement with previous work.[9, 62] More importantly, compared with the case of unsupported CaO, the presence of MgO also dramatically affected the crystallite size of CaO.

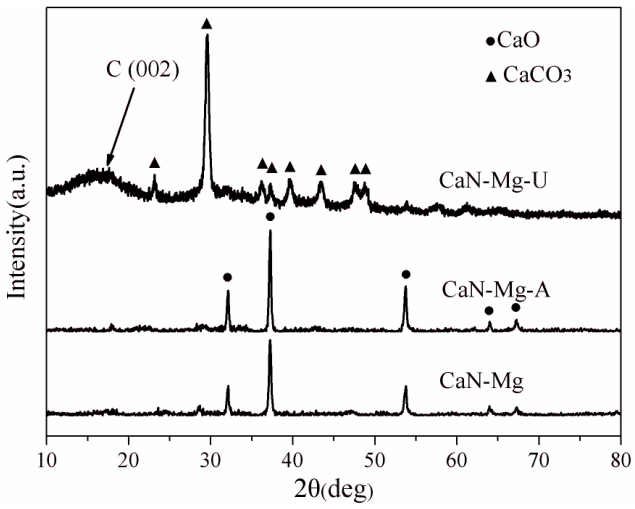

Fig. 6 compared XRD patterns of three samples

A carbon template also helps to reduce the particles size. As shown in Fig. 7, the carbon template appeared to co-exist as large and small sheet-like structure, suggesting that the addition of MgO allowed a pyrolysis process with inhomogeneous decomposition. The sheet-like architecture was well maintained in both Ca-Mg-A (Fig. 7b) and Ca-Mg (Fig. 7c). Their surfaces were highly macroporous but not as smooth as the case of the support (pure CaO), implying the deposition of MgO on the support surface. Here, both MgO-stabilized CaO samples produced relatively regular and smaller nano-sized CaO particles. In particular, the size of nano-particles obtained in Ca-Mg (Fig. 7c) was appreciably smaller for the two MgO-

stabilized CaO samples. Apparently, the carbon template and the deposition of MgO both served as dispersant to prevent growth of nano-sized CaO particles. Unlike the case of Ca-Mg-A, the high-resolution imagine and the TEM image of Ca-Mg (Fig. 7d) both reveals that particles in Ca-Mg were so well distributed in the sheet architecture that they were difficult to distinguish from each other even at the nanometer level. This observation provides a strong indication of excellent homogeneous mixing between MgO and CaO.

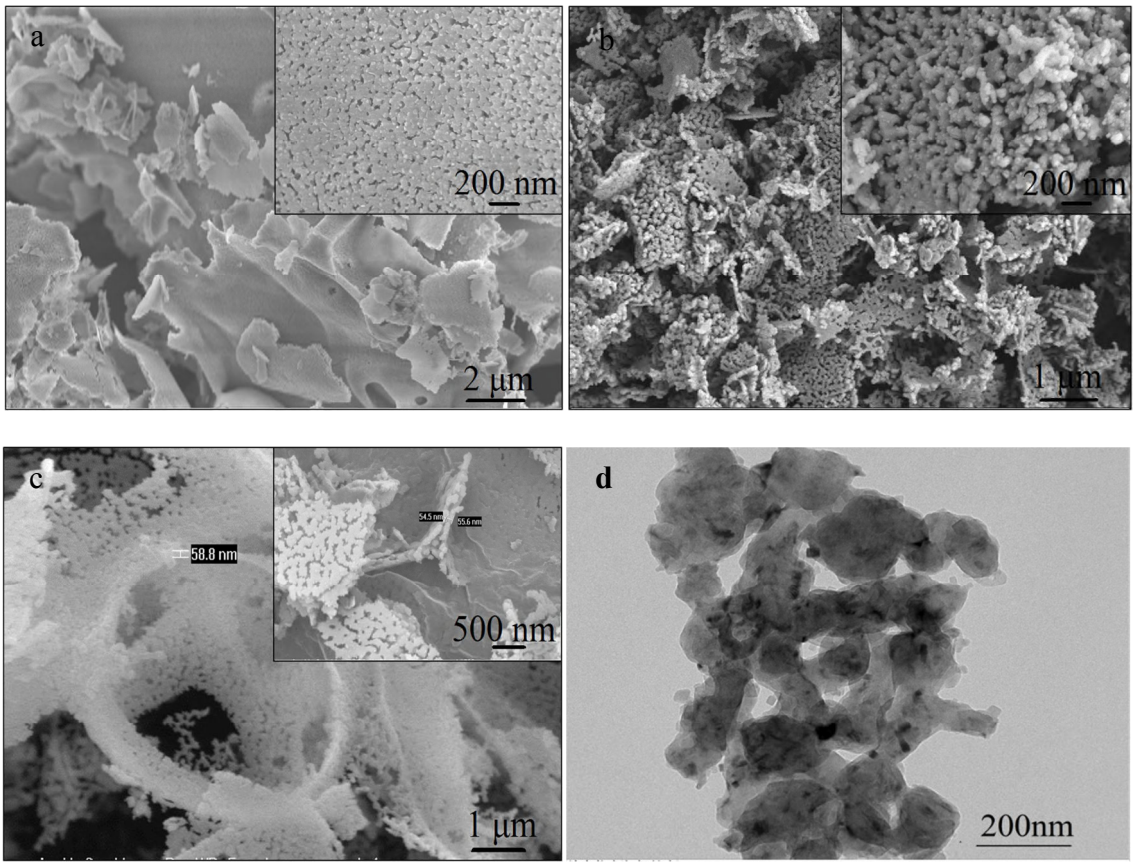

Fig. 7 SEM images of simples: (a) Ca-Mg-U, (b) fresh Ca-Mg-A, (c) fresh Ca-Mg

(d) TEM image of Ca-Mg.

The SEM/EDX elemental mapping images were further used to identify the composition distribution of Ca-Mg. As display in Fig. 8, both Ca and Mg filed all the mapping images, revealing an inhomogeneous distribution of the stabilizer (MgO) within the active material (CaO). Previous researchers[9, 58] proposed that the carbon template could beneficial for the compositional homogeneity of its products. To confirm this hypothesis, XRD and XPS

analysis were performed for the carbon template (Ca-Mg-U). Compared with the reference phrase of $CaCO_3$, the XRD patterns of the carbon template shifted to higher angles (Fig. 9a), suggesting that a Mg-doped calcite phase of $Mg_xCa_{1-x}CO_3$ (JPCD 086-2335) was produced. XPS (Fig. 9b) analyses also showed that the Ca-2p spectra of the carbon template displayed an obvious shifting as compared with the analytical pure $CaCO_3$, indicating that MgO may have inserted into the structure of $CaCO_3$ to form a solid solution. The above analyses clearly demonstrates that a solid solution is formed between MgO and calcite in the carbon template provided the possibility of homogeneous distribution property of products.

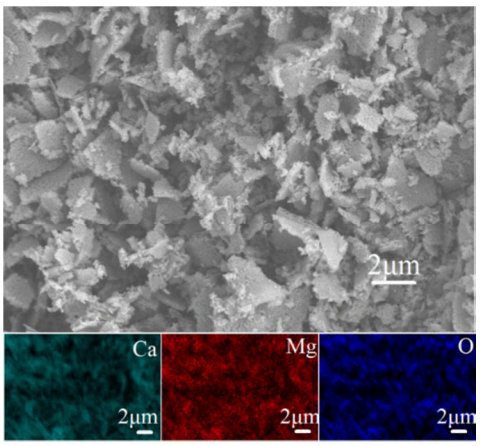

Fig. 8 SEM-mapping of Ca-Mg.

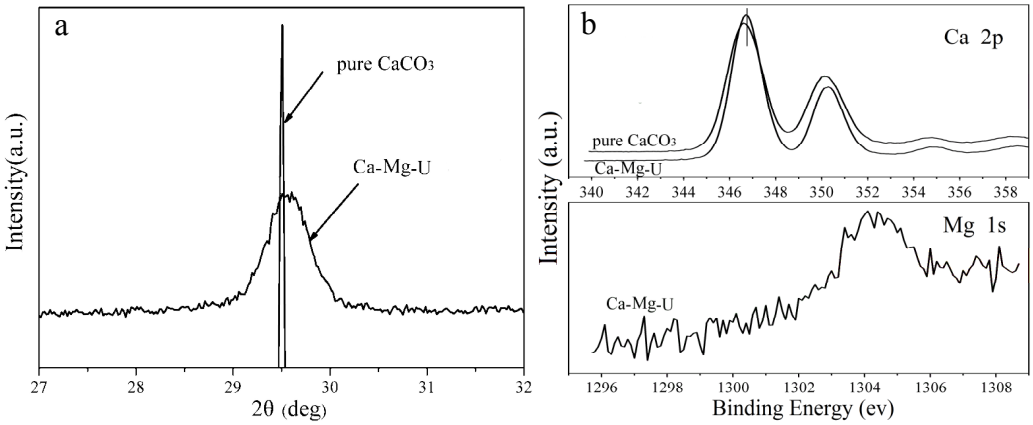

Fig. 9 XRD patterns (a) and XPS spectra of Ca-2p and Mg-1s (b) of Ca-Mg-U.

Fig. 10, illustrates schematically the pyrolysis of D-Glucose acid and nitrates in a simple

heating process under N_2. The pyrolysis occurring in a reducing atmosphere, N-doped carbon nanosheet is *situ* formed. At the same time, MgO-doped calcite can also be embedded in such carbon templates. Further removal of the template upon calcination under air, highly macroporous MgO-stabilized CaO nanosheets (~60 nm thick) with homogeneously mixing are obtained.

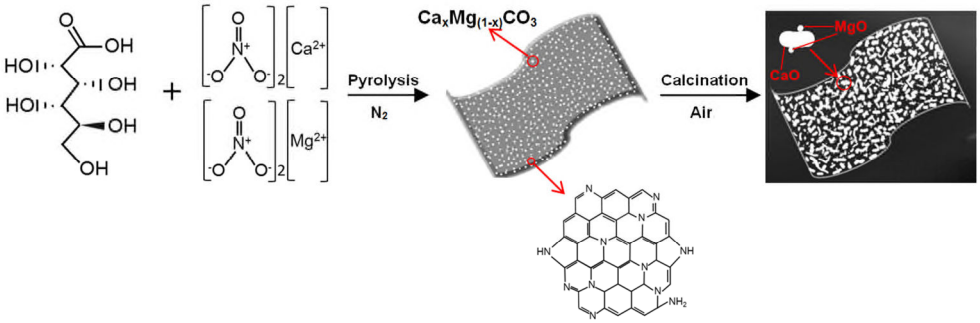

Fig. 10 Schematic of the individual synthesis steps to produce the MgO-stabilized CaO sorbents

Fig. 11a compared cyclic CO_2 capture performance of CaN, Ca-Mg-A and Ca-Mg. MgO containing sorbents exhibited a stable CO_2 uptake, whereas pure CaO sorbents revealed a characteristic decay in the CO_2 capture with repeated cycles. However, the initial CO_2 uptake of Ca-Mg-A in the absence of carbon template was rather lower than CaN due to the presence of inert stabilizer (MgO: T_T ~1290 °C). Fortunately, the CO_2 uptake of Ca-Mg approached that of CaN in the first four cycles. Moreover, it maintained remarkably high CO_2 uptake of 0.690 g/g even after 10 cycles. The carbonation profiles of these CaO sorbents were further examined. Here, compared with CaN, the carbonation rate in initial rapid chemically reaction stage for Ca-Mg became faster (Fig. 11b), most likely owing to its smaller nano-sizfed CaO particles and larger surface area (Table 2). Diffusion of CO_3^{2-} for Ca-Mg was also faster than Ca-Mg-A at the diffusion-stage due to its smaller CaO crystal size. The faster carbonation rate both in chemically reaction stage and diffusion-stag is very important for practical applications.[63] In light of these observations, both the presence of MgO and carbon template

are required concurrently to produce a superior CO_2 uptake performance (Fig. 11b).

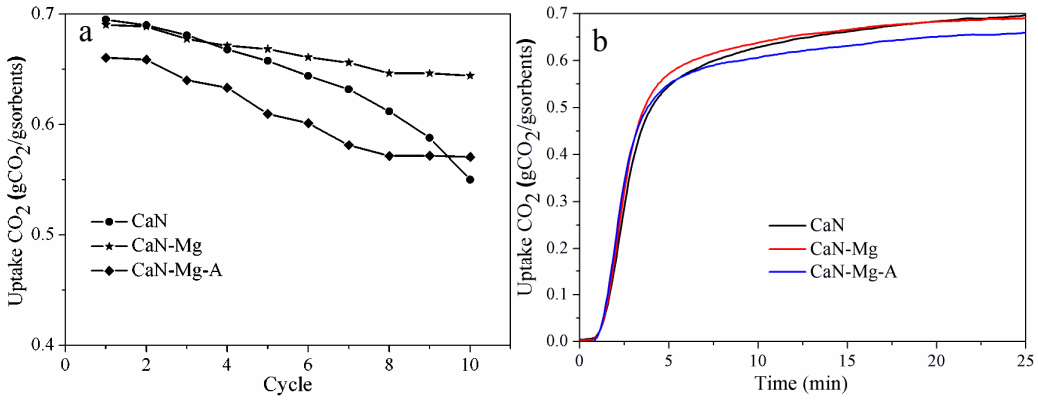

Fig. 11 Cyclic CO_2 capture performance of sorbents. (a) Cyclic CO_2 capture results of sorbents over 10 cycles, (b) The carbonation reaction on the first cycle.

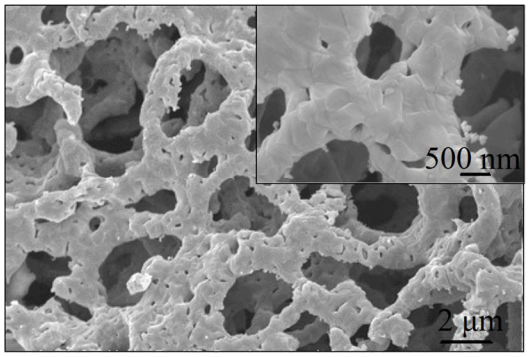

Fig. 12 The SEM imagines of cycled Ca-Mg.

The following three features of Ca-Mg contributed to its superior CO_2 uptake characteristics. First, with the help of N-doped carbon nanosheet template, agglomeration was prevented and in turn produced highly macroporous structure (larger specific surface area and pore volume), with abundant access areas for CO_2 uptake, which also mitigates the issue of meso-pore blockage in the initial cycle. Second, using a nanosheet-structured (~60 nm) sorbent as shown in Fig. 7c, the slow diffusion reaction stage was avoided. Third, a homogeneous mixing between MgO and CaO (at the nanometer level) was essential for a structural stabilization to resist sintering and further resulted in stable CO_2 uptake. More importantly, the highly macroporous and homogeneous nanocomposites are evidently

maintained during cyclic operation. The SEM images in Fig. 12 clearly demonstrate that the cycled Ca-Mg retained highly macroporous nanofibers to a large extent. The close-up view of the sheet showed that both MgO and CaO particles presented an inhomogeneous distribution because they were not easily distinguished with each other.

3.3 Other metallic oxides-stabilized CaO sorbents

To explore in more detail the benefits of the N-doped carbon template approach, several metallic oxides (ZrO_2, CeO_2 and Al_2O_3) in the form of metal nitrates were added as the stabilizers. The molar ratios of Ca to inserted metal ion are all 9/1. XRD patterns of these stabilized CaO samples are given in Fig. 13. The main crystalline phase identified in all these samples was CaO. However, different additional phases were also detected. For ZrO_2 and Al_2O_3 stabilized CaO, the stabilizers reached with CaO to yield $CaZrO_3$ and $CaAl_2O_4$, respectively. However, in the case of CeO_2-supported CaO, CeO_2 did not seem to form mixed oxides with CaO under the relevant operating conditions, which is in agreement with previous studies.[46] More importantly, the presence of stabilizers dramatically affected the crystallite size of CaO. As noted in Table 1, apart from the case of ZrO_2-stabilized CaO, all of these stabilizers can reduce the crystallite size of CaO.

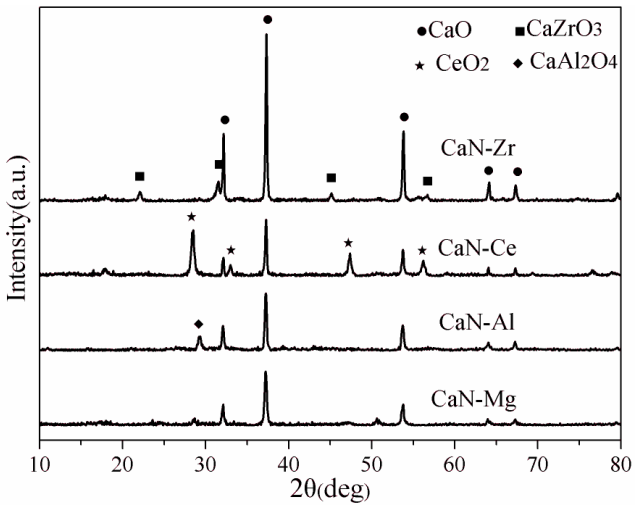

Fig. 13 XRD patterns of the samples

The morphology of these samples is shown in Fig. 14. All of stabilized CaO were

composed of ill-defined nanoparticles (50-200 nm). Furthermore, variation of stabilizers has a remarkable influence on the overall morphology of the sorbents. Ca-Zr (Fig. 14a) and Ca-Al (Fig. 14b) feature a rather similar morphology that is comprised of twisted and separated agglomerates. The close-up view (the insets) of Fig. 14a-b further reveals that Ca-Al present a smaller grain size (~100 nm) than the case of Ca-Zr (~200 nm). Compared with the nanosheet morphology of unsupported CaO, Ca-Zr and Ca-Al, all of which lost their sheet-like architecture, this may be due to the reaction between stabilizers and CaO as confirmed by XRD analysis. For Ca-Ce (Fig. 14c), only a certain degree of sheet-like architecture was kept, because the presence of CeO_2 may have had an inhibition effect on the formation of N-doped carbon nanosheet template under N_2.[64] The high-resolution imagine further showed that nano-sized coarse particles were covered by tiny particles.

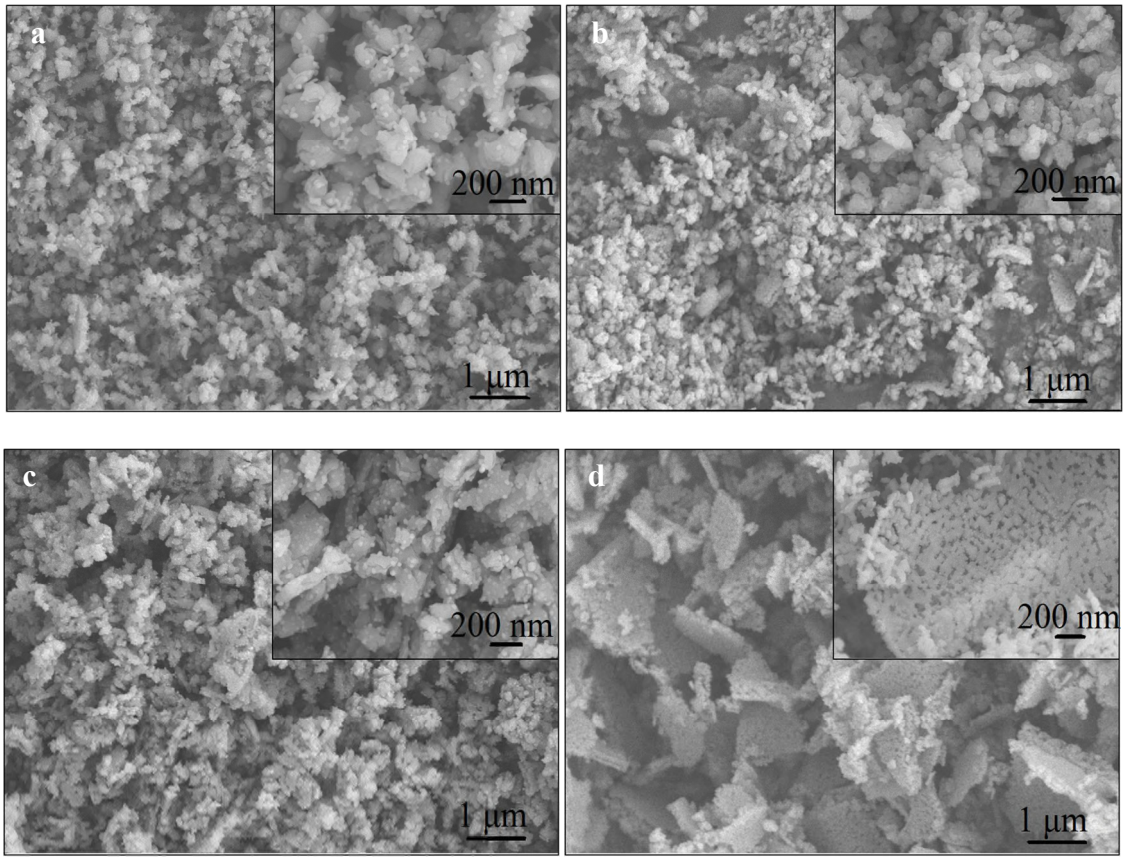

Fig. 14 SEM images of simples: (a) Ca-Zr, (b) Ca-Al, (c) Ca-Ce, (d) Ca-Mg.

The cyclic CO_2 uptake capacity of stabilized CaO is plotted in Fig. 15. Here, the initial

CO_2 uptake of Ca-Zr and Ca-Al was 0.56 g/g and 0.59 g/g, respectively, whereas unstabilized CaN had a CO_2 uptake of 0.705 g/g. The reduction in the initial CO_2 capacity was probably due to the formation of inert $CaZrO_3$ and $CaAl_2O_4$, which consumes some of the active CaO. Such stabilizers are known to act as a physical barrier to prevent sorbents from sintering, thus, the CO_2 capacity was maintained during 10 cycles as demonstrated by the fact that the uptake capacity of Ca-Al only decreased from 0.59 g/g to 0.55 g/g at 10 cycles. On the other hand, CeO_2 did not react with active CaO. However, the CO_2 uptake of Ca-Ce remained at levels of 0.56 g/g over the 10 reaction cycles. The stable but low CO_2 uptake of Ca-Ce agree with the previously reported values for CeO_2-stabilized CaO. More importantly, compared with unsupported CaO, the cyclic stability of all stabilized CaO improves remarkably, suggesting that the N-doped carbon template remains available over the 10 cycles in several stabilizers. It should be also noted that Ca-Mg showed the best CO_2 uptake performance among these stabilized CaO, possibly attributable to its smallest grain size (Table 1), and a well-preserved nanosheet-like structure which can be seen for the smallest nanoparticles (Fig. 14d).

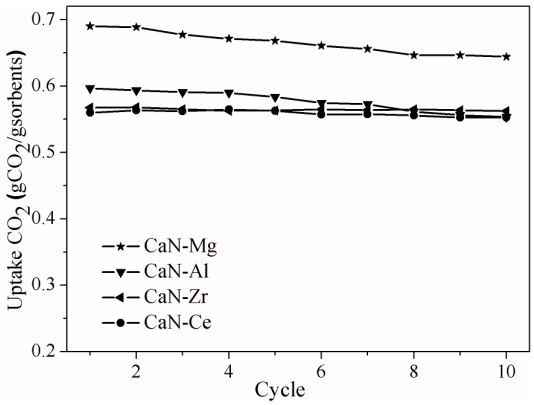

Fig. 15 Cyclic CO_2 capture performance of the sorbents.

4 Conclusions

In this work, we have developed a simple cost-effective and scalable approach to produce highly efficient MgO-stabilized, CaO sorbents. The sacrificial N-doped carbon nanosheet template was formed through *in situ* pyrolysis of organic acid and metal nitrate in a

simple heating process under N_2. The presence of a carbonaceous template not only prevented crystallite growth of $CaCO_3$ but also served as a nanosheet temple to form highly porous CaO nanosheets. More importantly, for the pyrolysis of gluconic acid and a mixture of $Ca(NO_3)_2/Mg(NO_3)_2$, a solid solution between $CaCO_3$ and MgO was produced which ensured homogeneous mixing of Ca and Mg in the porous MgO-stabilized CaO nanosheet (~60 nm thick). In particular, the cycled MgO-stabilized CaO sorbent also showed macroporous and homogeneous nanofibers. These features were critical to achieve minimal diffusion limitations, mitigate sintering, and stabilize the structure of the sorbents. Thus, fast adsorption rate, high capacities and remarkably improved cyclic performance of CaO sorbents were obtained. Using this novel route, a MgO content as low as 10 mol% was sufficient to retain CO_2 uptake of 0.65 g/g (corresponding to a capacity retention of 89.9%) after 10 cycles under realistic operating conditions. In addition, the N-doped carbon template is able to form a wide range of porous and nanostructured stabilized-CaO sorbents with stable CO_2 uptakes.

Acknowledgment

This work is supported by the Outstanding Teacher Overseas Research Project and the Fundamental Research Funds for Talents Cultivation Project of China University of Mining and Technology.

References

1. M. E. Boot-Handford, J. C. Abanades, E. J. Anthony, M. J. Blunt, S. Brandani, N. Mac Dowell, J. R. Fernández, M.-C. Ferrari, R. Gross, J. P. Hallett, R. S. Haszeldine, P. Heptonstall, A. Lyngfelt, Z. Makuch, E. Mangano, R. T. J. Porter, M. Pourkashanian, G. T. Rochelle, N. Shah, J. G. Yao and P. S. Fennell, *Energy Environ. Sci.*, 2014, **7**, 130-189.
2. D. P. Hanak, E. J. Anthony and V. Manovic, *Energy Environ. Sci.*, 2015, **8**, 2199-2249.
3. M. Bui, C. S. Adjiman, A. Bardow, E. J. Anthony, A. Boston, S. Brown, P. S. Fennell, S. Fuss, A. Galindo, L. A. Hackett, J. P. Hallett, H. J. Herzog, G. Jackson, J. Kemper, S. Krevor, G. C. Maitland, M. Matuszewski, I. S. Metcalfe, C. Petit, G. Puxty, J. Reimer, D. M. Reiner, E. S. Rubin, S. A. Scott, N. Shah, B. Smit, J. P. M. Trusler, P. Webley, J. Wilcox and N. Mac Dowell, *Energy Environ. Sci.*, 2018, **11**, 1062-1176.
4. J. Blamey, E. J. Anthony, J. Wang and P. S. Fennell, *Prog. Energy Combust. Sci.*, 2010, **36**, 260-279.
5. J. Wang, L. Huang, R. Yang, Z. Zhang, J. Wu, Y. Gao, Q. Wang, D. O'Hare and Z. Zhong,

Energy Environ. Sci., 2014, **7**, 3478-3518.
6. S. I. Garces-Polo, J. Villarroel-Rocha, K. Sapag, S. A. Korili and A. Gil, *Chem. Eng. J.*, 2018, **332**, 24-32.
7. L. K. G. Bhatta, S. Subramanyam, M. D. Chengala, S. Olivera and K. Venkatesh, *J. Clean. Prod.*, 2015, **103**, 171-196.
8. C. Su, L. Duan, F. Donat and E. J. Anthony, *Appl. Energy*, 2018, **210**, 117-126.
9. K. Wang, X. Hu, P. Zhao and Z. Yin, *Appl. Energy*, 2016, **165**, 14-21.
10. Y. Li, X. Ma, W. Wang, C. Chi, J. Shi and L. Duan, *Chem. Eng. J.*, 2017, **316**, 438-448.
11. Y. Xu, C. Luo, Y. Zheng, H. Ding and L. Zhang, *Energy Fuels*, 2016, **30**, 3219-3226.
12. B. Alcantar-Vazquez, Y. Duan and H. Pfeiffer, *Ind. Eng. Chem. Res.*, 2016, **55**, 9880-9886.
13. X.-S. Yin, M. Song, Q.-H. Zhang and J.-G. Yu, *Ind. Eng. Chem. Res.*, 2010, **49**, 6593-6598.
14. I. Ham-Liu, J. Arturo Mendoza-Nieto and H. Pfeiffer, *Journal of CO_2 Utilization*, 2018, **23**, 143-151.
15. H. A. Lara-Garcia, P. Sanchez-Camacho, Y. Duan, J. Ortiz-Landeros and H. Pfeiffer, *J. Phys. Chem. C*, 2017, **121**, 3455-3462.
16. M. Erans, V. Manovic and E. J. Anthony, *Appl. Energy*, 2016, **180**, 722-742.
17. J. M. Valverde, P. E. Sanchez-Jimenez and L. A. Perez-Maqueda, *Appl. Energy*, 2015, **138**, 202-215.
18. A. M. Kierzkowska, R. Pacciani and C. R. Müller, *ChemSusChem*, 2013, **6**, 1130-1148.
19. W. Liu, H. An, C. Qin, J. Yin, G. Wang, B. Feng and M. Xu, *Energy Fuels*, 2012, **26**, 2751-2767.
20. V. Manovic and E. J. Anthony, *Energy Fuels*, 2010, **24**, 5790-5796.
21. J. C. Abanades, E. J. Anthony, J. Wang and J. E. Oakey, *Environ. Sci. Technol.*, 2005, **39**, 2861-2866.
22. I. Martinez, G. Grasa, R. Murillo, B. Arias and J. C. Abanades, *Energy Fuels*, 2011, **25**, 1294-1301.
23. P. Sun, J. R. Grace, C. J. Lim and E. J. Anthony, *Ind. Eng. Chem. Res.*, 2008, **47**, 2024-2032.
24. V. Manovic and E. J. Anthony, *Environ. Sci. Technol.*, 2008, **42**, 4170-4174.
25. P. Lan and S. Wu, *Fuel*, 2015, **143**, 9-15.
26. A. Perejon, L. M. Romeo, Y. Lara, P. Lisbona, A. Martinez and J. Manuel Valverde, *Appl. Energy*, 2016, **162**, 787-807.
27. B. Arias, G. S. Grasa, M. Alonso and J. C. Abanades, *Energy Environ. Sci.*, 2012, **5**, 7353-7359.
28. B. González, J. Blamey, M. J. Al-Jeboori, N. H. Florin, P. T. Clough and P. S. Fennell, *Chem. Eng. Process.*, 2016, **103**, 21-26.
29. Y. Hu, W. Liu, J. Sun, M. Li, X. Yang, Y. Zhang, X. Liu and M. Xu, *Fuel*, 2016, **167**, 17-24.
30. Y.-j. Li, C.-s. Zhao, L.-b. Duan, C. Liang, Q.-z. Li, W. Zhou and H.-c. Chen, *Fuel Process. Technol.*, 2008, **89**, 1461-1469.
31. L. Duan, C. Su, M. Erans, Y. Li, E. J. Anthony and H. Chen, *Ind. Eng. Chem. Res.*, 2016, **55**, 10294-10300.
32. M. Erans, F. Cerciello, A. Coppola, O. Senneca, F. Scala, V. Manovic and E. J. Anthony, *Fuel*, 2017, **187**, 388-397.
33. J. Sun, W. Liu, H. Chen, Y. Zhang, Y. Hu, W. Wang, X. Li and M. Xu, *Proc. Combust. Inst.*, 2017, **36**, 3977-3984.
34. Y. Xu, H. Ding, C. Luo, Y. Zheng, Y. Xu, X. Li, Z. Zhang, C. Shen and L. Zhang, *Chem. Eng. J.*, 2018, **334**, 2520-2529.
35. M. Broda, A. M. Kierzkowska and C. R. Mueller, *Adv. Funct. Mater.*, 2014, **24**, 5753-5761.
36. L. Li, D. L. King, Z. Nie and C. Howard, *Ind. Eng. Chem. Res.*, 2009, **48**, 10604-10613.
37. K. Wang, D. Han, P. Zhao, X. Hu, Z. Yin and D. Wu, *Thermochim. Acta*, 2015, **614**, 199-206.
38. K. Wang, X. Guo, P. Zhao and C. Zheng, *Appl. Clay Sci.*, 2010, **50**, 41-46.
39. Y. Li, M. Su, X. Xie, S. Wu and C. Liu, *Appl. Energy*, 2015, **145**, 60-68.
40. Z. S. Li, N. S. Cai, Y. Y. Huang and H. J. Han, *Energy Fuels*, 2005, **19**, 1447-1452.
41. V. Manovic and E. J. Anthony, *Environ. Sci. Technol.*, 2009, **43**, 7117-7122.
42. R. Han, J. Gao, S. Wei, Y. Su and Y. Qin, *J. Mater. Chem. A*, 2018, **6**, 3462-3470.
43. A. Antzara, E. Heracleous and A. A. Lemonidou, *Appl. Energy*, 2015, **156**, 331-343.

44. M. Zhao, M. Bilton, A. P. Brown, A. M. Cunliffe, E. Dvininov, V. Dupont, T. P. Comyn and S. J. Milne, *Energy Fuels*, 2014, **28**, 1275-1283.
45. M. Broda and C. R. Müller, *Fuel*, 2014, **127**, 94-100.
46. S. Wang, S. Fan, L. Fan, Y. Zhao and X. Ma, *Environ. Sci. Technol.*, 2015, **49**, 5021-5027.
47. J. C. Abanades and D. Alvarez, *Energy Fuels*, 2003, **17**, 308-315.
48. D. Alvarez and J. C. Abanades, *Ind. Eng. Chem. Res.*, 2005, **44**, 5608-5615.
49. R. Barker, *J. Appl. Chem. Biotechnol.*, 1973, **23**, 733-742.
50. P. Lan and S. Wu, *Chem. Eng. Technol.*, 2014, **37**, 580-586.
51. S. F. Wu and Y. Q. Zhu, *Ind. Eng. Chem. Res.*, 2010, **49**, 2701-2706.
52. N. J. Amos, M. Widyawati, S. Kureti, D. Trimis, A. I. Minett, A. T. Harris and T. L. Church, *J. Mater. Chem. A*, 2014, **2**, 4332-4339.
53. C.-C. Li, U.-T. Wu and H.-P. Lin, *J. Mater. Chem. A*, 2014, **2**, 8252-8257.
54. Z. Sun, M. H. Sedghkerdar, J. Saayman, N. Mahinpey, N. Ellis, D. Zhao and S. Kaliaguine, *J. Mater. Chem. A*, 2014, **2**, 16577-16588.
55. F.-Q. Liu, W.-H. Li, B.-C. Liu and R.-X. Li, *J. Mater. Chem. A*, 2013, **1**, 8037-8044.
56. M. Broda and C. R. Mueller, *Adv. Mater.*, 2012, **24**, 3059-3064.
57. H. Ping and S. Wu, *ACS Sustainable Chem. Eng.*, 2016, **4**, 2047-2055.
58. M. A. Naeem, A. Armutlulu, Q. Imtiaz, F. Donat, R. Schäublin, A. Kierzkowska and C. R. Müller, *Nat. Commun*, 2018, **9**, 2408.
59. P. T. Clough, M. E. Boot-Handford, M. Zhao and P. S. Fennell, *Fuel*, 2016, **186**, 708-713.
60. P. Zhao, J. Sun, Y. Li, K. Wang, Z. Yin, Z. Zhou and Z. Su, *Energy Fuels*, 2016, **30**, 7543-7550.
61. X. Liu and M. Antonietti, *Adv. Mater.*, 2013, **25**, 6284-6290.
62. C. Rodriguez-Navarro, K. Kudlacz and E. Ruiz-Agudo, *Am. Mineral.*, 2012, **97**, 38-51.
63. A. Perejón, L. M. Romeo, Y. Lara, P. Lisbona, A. Martínez and J. M. Valverde, *Appl. Energy*, 2016, **162**, 787-807.
64. M. M. Hossain, *Int. J. Hydrogen Energy*, 2018, **43**, 6088-6095.
.